Variable Coherence Microscopy: a Rich Source of Structural Information from Disordered Materials

M. M. J. TREACY[a]* AND J. M. GIBSON[b]

[a]*NEC Research Institute, 4 Independence Way, Princeton, NJ 08540, USA, and* [b]*University of Illinois, Department of Physics, 1110 W Green St, Urbana, IL 61801, USA. E-mail: treacy@research.nj.nec.com*

Abstract

Variable coherence microscopy, a tool for quantitative analysis of structural fluctuations in disordered materials, is introduced. The method involves transmission electron microscopy of thin films and uses hollow-cone illumination. Experiments were performed on annealed evaporated amorphous germanium. Although many aspects of the data agree with the continuous random network model, there is experimental evidence for additional medium-range structure on the 10–20 Å scale.

1. Introduction

In this paper, we introduce a new approach to electron microscopy of disordered materials, which we call variable coherence microscopy. There are two key aspects: firstly, we rely on quantitative measurement of image statistics; secondly, we use controlled partial spatial coherence in dark-field images as a variable that can tune into structural details. We develop a theory of the technique and show experimental results for evaporated amorphous germanium thin films. Using a computer model of amorphous Ge, we simulate the experimental results and show that the model, a continuous random network (CRN), is only partially adequate to explain our observations. Although the fluctuations in short-range order are in reasonable agreement with the CRN, we identify medium-range order in our samples not represented in the CRN model. We propose three directions for further research: development of better models; more extensive experiments on other amorphous samples, including Ge; and development of methods to extract microstructural parameters, such as pair–pair correlation functions, directly from the data.

The introduction of the continuous random network model by Zachariasen (1932) was a major intellectual achievement in rationalizing the structure of network glasses. The basic concept was that short-range order in covalent glasses should be very similar to that in crystalline phases, dictated by the chemical-bonding geometry. However, slight distortions of the basic units could lead to removal of long-range order and the formation of an amorphous phase. Structural measurements of amorphous materials have relied almost exclusively on diffraction. The diffracted intensity is closely related to the Fourier transform of the pair correlation function, otherwise known as the radial distribution function (RDF) (Warren, 1959). This relationship is conditional on assumptions of isotropy and homogeneity throughout the scattering volume. Bell & Dean (1972) built the first CRN model for vitreous SiO_2 that agreed well with experimental data. Later, Polk (1971) built a CRN model for amorphous elemental semiconductors, Si and Ge, which also agreed well with experiment, especially after minimization of the stress energy in the model (Polk & Boudreaux, 1973).

The early CRN models of Polk and Bell & Dean were generated by hand, whereas in more recent years efficient computer algorithms have been developed to generate larger CRN models. Good recent examples of these include Gladden (1990) for SiO_2 and Wooten, Winer & Weaire (1985) for Si and Ge. Although the CRN models have been successful in describing both structural and other features of amorphous materials, there are properties that they do not fully explain. These include thermal vibration, density, diffusion and the existence of a 'first sharp diffraction peak' (Elliott, 1992). As a result of these observations, there has been some controversy over the years on the existence of 'medium-range order' in amorphous materials, which is not included in the simple CRN model.

Other techniques to probe structure directly in glasses have been developed – such as Raman spectroscopy, which probes local phonons. One of the techniques that appeared most promising at the outset is high-resolution transmission electron microscopy (TEM). In principle, the electron microscope allows direct visualization of the structure in thin foils and appeared to offer additional insights. Early papers, apparently showing evidence for lattice planes in bright- and dark-field images, were later shown to be probable statistical effects of the image-formation process (Chaudhari & Graczyk, 1973). The most severe problem identified in this process was not the limited resolution of the electron microscope but the projection required through the typical thin samples used. In this regard, the appearance of false crystalline regions in TEM images is similar to the illusion of 'ghosts' in radar images – both can arise from statistical scattering by a random phase grating.

Although much useful work has since been done using electron microscopy for non-atomic scale structural analysis, skepticism has set in regarding qualitative presentation of high-resolution images showing local atomic order in amorphous thin films. Nevertheless, as demonstrated by several more recent studies, direct imaging clearly offers additional information on microstructure over averaged diffraction – for example, the assumptions of isotropy and homogeneity can be scrutinized. Krivanek, Gaskell & Howie (1976) found qualitative evidence for medium-range order on the 15 Å scale in amorphous carbon by comparing micrographs before and after randomizing the phases of the image Fourier components. Using computer-digitized video micrographs, Fan & Cowley (1985, 1988) demonstrated more quantitative analytical methods based on auto-correlation analysis to derive an average local correlation function (Fan & Cowley, 1985) and information theory to delineate the non-random image features (Fan & Cowley, 1988). Progress is further facilitated today by efficient linear electron detector arrays and fast digital image storage and analysis.

There are many different instrumental conditions that can be controlled during electron microscopy at moderately high resolution. Based on earlier work (Gibson & Howie, 1978), we chose to use the partial spatial coherence of the electron illumination as a variable parameter for probing statistics of images – defining variable coherence microscopy. It was shown that reduced coherence could partially compensate for the projection problem by limiting the local volume in which correlations are probed. This concept was explored in more detail recently by Treacy & Gibson (1993) and Jesson & Pennycook (1993), who showed both experimentally and theoretically that the coherence volume can be reproducibly controlled experimentally. A convenient method for coherence control uses annular dark-field imaging, which is similar to the 'Z-contrast' technique in the scanning transmission electron microscope (STEM). In our experiments, we used the equivalent TEM hollow-cone dark-field method, which readily permits continuous variation of coherence.

We have developed a theoretical interpretation of variable coherence microscopy showing that the method gives insight beyond the simple atomic pair correlation function familiar from diffraction. The procedure explores the higher-order pair–pair correlation function, which we believe is more sensitive to medium-range order.

For the experiments reported here, we prepared films of evaporated amorphous Ge, which showed diffraction patterns closely consistent with CRN models. Our data analysis was paralleled with simulations of our experiments using a CRN model. Results show that, although the CRN model is an adequate description of short-range order in our samples, we observe pronounced medium-range structure not contained in the CRN model. We also conclude that the technique is a rich source of new structural information about disordered materials in general. We point the way towards future work to resolve the discrepancies and directly obtain structural information from our method.

2. Theory

In the variable coherence technique, images are taken in dark field. Although we develop a theory for partially coherent illumination, we begin with the more familiar coherent case. Because we are interested only in moderate image resolution and relatively thin amorphous films, we will ignore the microscope aberrations and use the kinematical scattering theory (Gibson, 1994). The groundwork for the following treatment is covered in more detail in Treacy & Gibson (1993, 1995). The specimen is treated as an assembly of identical atoms at positions r_j. The illumination is a tilted plane wave, characterized by wave vector κ, and the scattered waves are collected by an objective aperture centered on the optic axis. The kinematical coherent dark-field-image intensity at specimen position r is well approximated by

$$I(r, \kappa) = f^2(\kappa) \sum_j \sum_l a_j(r - r_j) a_l^*(r - r_l) \exp(-2\pi i \kappa \cdot r_{jl}).$$

(1)

The quantity $r_{jl} = r_l - r_j$ represents the position vector of atom l relative to atom j. $f(\kappa)$ is the atomic scattering factor. The $a_j(r - r_j)$ are related to the image wavefunctions of the individual atoms and are given by

$$a_j(r - r_j) = i\lambda \iint_{obj} \exp(2\pi i q \cdot (r - r_j)) d^2q$$

$$= i\lambda \pi Q^2 A_j,$$

(2)

where λ is the electron wavelength and Q is the radius of the objective aperture. The quantity A_j^2, where

$$A_j = 2J_1[2\pi Q|(r - r_j)|]/2\pi Q|(r - r_j)|,$$

(3)

is the well known Airy intensity distribution for diffraction from a circular aperture, J_1 being the Bessel function of the first order.

The mean image intensity in the coherent dark field, $\langle I(\kappa) \rangle$, is given by averaging (1) over the image area M:

$$\langle I(\kappa) \rangle = [\lambda^2 f^2(\kappa)/M] \sum_j \sum_l \iint \exp[2\pi i(q - \kappa) \cdot r_{jl}] d^2q$$

$$= [\pi Q^2 \lambda^2 f^2(\kappa)/M] \sum_j \sum_l A_{jl} \exp(-2\pi i \kappa \cdot r_{jl}),$$

(4)

where now we are using $A_{jl} = 2J_1(2\pi Q r_{jl})/2\pi Q r_{jl}$. Since $q - \kappa$ is the total scattering vector experienced by the beam at q in the objective aperture, the average image intensity is nothing more than the total diffracted

intensity accepted by the objective aperture, averaged over the image area. Therefore, we learn no more from the average image intensity than we do from the diffraction pattern.

Now consider the second moment of the image intensity distribution, $\langle I^2(\kappa)\rangle$. From (1), this is given by

$$\langle I^2(\kappa)\rangle = [f^4(\kappa)/M] \sum_j \sum_l \sum_m \sum_n \exp[-2\pi i\kappa \cdot (r_{jl} + r_{mn})]$$

$$\times \iint_{image} a_j a_l^* a_m a_n^* \, d^2r, \qquad (5)$$

which simplifies to

$$\langle I^2(\kappa)\rangle = [\pi^3 Q^6 \lambda^4 f^4(\kappa)/M] \sum_j \sum_l \sum_m \sum_n A_{jn} A_{nl} A_{mn}$$

$$\times \exp[-2\pi i\kappa \cdot (r_{jl} + r_{mn})]. \qquad (6)$$

We define the speckle contrast in terms of the normalized variance V, which from (4) and (6) is

$$V = \langle I^2(\kappa)\rangle / \langle I(\kappa)\rangle^2 - 1$$

$$= N_0 \frac{\sum_{j,l,m,n} A_{jn} A_{nl} A_{mn} \exp[-2\pi i\kappa \cdot (r_{jl} + r_{mn})]}{\sum_{p,q,r,s} A_{pq} A_{rs} \exp[-2\pi i\kappa \cdot (r_{pq} + r_{rs})]} - 1, \qquad (7)$$

where $N_0 = \pi Q^2 M$, the number of resolution elements, which is the number of pixels in an optimally sampled image. The standard deviation S is, as usual, equal to $V^{1/2}$. Examination of (7) shows that speckle is maximized when similar atom pairs jl and mn are localized within the same column, as determined by the characteristic width of the Airy discs $A_{jn} A_{nl}$, which mediate the coupling of the jl and mn pair, and the specimen thickness. Thus, the speckle reveals a higher-order pair–pair correlation, and contains additional information beyond the first-order pair statistics obtained from diffraction.

Following Treacy & Gibson (1993), (7) is readily generalized to the partially coherent illumination case. The result is equivalent to replacing the terms $\exp(-2\pi i\kappa \cdot r_{jl})$ by a modified coherence strength term F_{jl}. Thus, more generally, V can be expressed as

$$V = N_0 \frac{\sum_{j,l,m,n} A_{jn} A_{nl} A_{mn} F_{jl} F_{mn}}{\sum_{p,q,r,s} A_{pq} A_{rs} F_{pq} F_{rs}} - 1 \qquad (8)$$

with $F_{jl} = \exp[-2\pi i\kappa \cdot r_{jl}]$ in the coherent limit. In the case of a hollow cone of illumination subtending collection vectors k_1 to k_2, the F_{jl} are given by (Treacy & Gibson, 1993)

$$F_{jl} = \left\{ \int_{k_1}^{k_2} J_0(2\pi k\sigma_{jl}) \exp(2\pi i\gamma z_{jl}) f^2(\kappa) \right.$$

$$\left. \times \exp[-2M(\kappa)]w(\kappa)\kappa \, d\kappa \right\}$$

$$\times \left\{ \int_{k_1}^{k_2} f^2(\kappa)w(\kappa)\kappa \, d\kappa \right\}^{-1}. \qquad (9)$$

Here, κ and r_{jl} have been decomposed into their components (k, γ) and (σ_{jl}, z_{jl}), perpendicular and parallel to the optic axis (Treacy & Gibson, 1993). For small-angle scattering, $\lambda k \ll 1$ and $\gamma = \lambda k^2/2$. $M(\kappa)$ is the isotropic Debye–Waller temperature factor and $w(\kappa)$ is a weighting factor that allows for the possibility that not all angular zones in the annular illumination are equally intense. The partial spatial coherence has the effect of localizing the function F_{jl}, particularly when a wide range of illumination vectors k are present, reducing the effect of long-range interference (Treacy & Gibson, 1993). For a narrow hollow cone, F_{jl} has characteristic length scales of $1/k$ perpendicular to the optic axis and $1/\gamma$ parallel to the optic axis. Since $\gamma \ll k$, F_{jl} describes a narrow volume that is elongated and oscillatory along the optic axis.

Oscillations in the standard deviation S versus k can occur due to correlations in the electron-beam direction z, as well as correlations in the plane normal to z, which is σ. In principle, these can be distinguished because of their differing dependence on electron wavelength as described above.

Fig. 1 illustrates the importance of pair–pair correlations in differentiating structural configurations. The three configurations sketched each involves two identical atomic pairs. It is assumed for clarity that the F_{jl} term for each of these pairs is unity – that is, each atom of the pair lies within the same coherence volume (shaded cylinders). In this figure, the image resolution is represented by an Airy disc (the unshaded cylinders, essentially A_{jl}) that here is shown as being significantly wider than the coherence volume. The two numeric columns in the figure list the number of non-zero terms in the numerator (labeled 'Speckle') and denominator (labeled 'Diffraction' but is actually the square of the total diffracted intensity) of (8) for the image intensity variance V. Since there are four atoms in this hypothetical specimen, and each column corresponds to a quadruple sum over j, l, m and n, there is a total of $4^4 = 256$ possible terms contributing to both the numerator and denominator. In the first configuration, all four atoms align in a column such that they all fall within the same coherence volume, as well as within the same Airy disc. Thus, all 256 terms can contribute significantly to both the numerator and denominator. In the second configuration, the two pairs lie in different coherence volumes, but they all lie under the same Airy disc. Thus, for atom pairs (1, 2) and (3, 4), intra-column terms of the type F_{11} and $F_{12} = F_{21}$ are non-zero, but inter-column terms such as F_{13} etc. are zero. This provides for 16 non-zero 'diffraction' terms out of a

possible 256 and 64 speckle terms out of a possible 256. In the third configuration, the two pairs lie in different coherence volumes and are under different Airy discs. This provides for additional restraints, such as A_{13} etc. being zero. This latter restraint has no effect on the total number of non-zero 'diffraction' terms, 16, but halves the number of 'speckle' terms to 32. In this manner, the image variance is sensitive to pair–pair correlations in the specimen, whereas the diffracted intensity (mean image intensity) is sensitive to pair correlations alone.

Full realistic calculations of the standard deviation $S = V^{1/2}$ using (8) require a very large number of atoms (of the order of 10^6) and are therefore numerically intensive. To facilitate the interpretation of our data, we have performed simulations of S using a simpler approximation. We pick a cluster of atoms (≤ 5000) and calculate for a specific orientation the scattered intensity under the appropriate coherence conditions. The model is then rotated to a sequence of angles θ (about one axis perpendicular to the optic axis) in $1°$ steps. The mean and mean-square intensities are tracked. Before S is calculated, the intensity sums are weighted by a factor $2\pi\theta$ to account for random spatial orientation of the clusters. This latter factor favors σ_{jl} correlations for isotropic structures at medium angles – contrary

to previous assumptions (Gibson & Howie, 1978). On comparing with the experimental data, the simulations should be weighted by two additional factors – the expected number of clusters in the film thickness, N_c, and the number of resolution elements in an image pixel, N_p. The correction factor is $1/(N_cN_p)^{1/2}$.

Note that the speckle variance is only one of many possible parameters to examine. But even this simple measure shows rich structure, as we shall see.

3. Experimental

Samples of amorphous Ge were prepared by vacuum evaporation of a 99.999% purity Ge target in a bell jar with base pressure 2.6×10^{-5} Pa. Films were deposited at a rate of $\sim 2 \text{ Å s}^{-1}$ onto Si substrates coated with poly(methyl methacrylate) (PMMA) and held near room temperature. Film thickness was monitored during deposition with a quartz crystal, which was calibrated from thick deposits by a profilometer. Thicknesses are accurate to about 10%. Ge thin films were floated onto Cu grids by dissolving the PMMA in acetone. Specimens were further cleaned in an acetone still by supporting them on a Cu gauze that was located at the same level as the acetone dew point. In this way, pure hot acetone condenses onto the specimens and then drips off leaving minimal residue. Ge films were examined before and after *in situ* thermal annealing at ~ 573 K for 30 min in vacuum.

We used a Hitachi H9000 NAR TEM for all experiments, operated at either 100 or 200 kV accelerating voltage. Hollow-cone illumination was created using a quadrature oscillator condenser scanning system (Krakow & Howland, 1976) at a frequency of 53 Hz. The angular width of the hollow cone was set by the condenser aperture angular width. The rastered annulus is therefore non-uniformly filled, with the intensity strongest at the central angle and falling off as $[1 - (\Delta\theta/\theta)^2]^{1/2}$, where θ is the angular radius of the condenser aperture and $\Delta\theta$ is the angle relative to the aperture center. The hollow-cone semi-angle was calibrated using diffraction from a polycrystalline Al foil. This calibration is sensitive to objective-lens current, which was carefully controlled in our experiments. Since the plane of the hollow-cone pivot point changes with cone angle, care was taken in our experiments to ensure that the pivot point was always coincident with the specimen plane. Otherwise, the angular calibration can be strongly affected. The smallest hollow-cone angle is determined by the angular radius of the objective aperture. Thus, the lowest-angle data required the use of the smallest objective apertures with a concomitant reduction in image spatial resolution. Images were recorded at calibrated magnifications of 27 700× at 200 kV and 37 600× at 100 kV on a cooled slow-scan Gatan CCD camera (model 690) with a pixel size of 24 μm. The equivalent pixel size at the sample

Configuration	Number of terms	
	Diffraction $\sum_{jlmn} A_{jl}A_{mn}F_{jl}F_{mn}$	Speckle $\sum_{jlmn} A_{jn}A_{nl}A_{mn}F_{jl}F_{mn}$
	256	256
	16	64
	16	32

Fig. 1. Three hypothetical specimen configurations that emphasize the importance of pair–pair correlations in differentiating structural configurations. The three configurations sketched each involve two identical atomic pairs. The coherence volumes are represented by shaded cylinders and the instrumental resolution, the Airy disc, by the wider unshaded cylinders. The two columns in the figure list the number of non-zero terms in the numerator (labeled 'Speckle') and denominator (labeled 'Diffraction') of equation (8) for the image intensity variance V. Configurations 2 and 3 reveal that the image variance is sensitive to pair–pair correlations in the specimen, whereas the diffracted intensity (mean image intensity) is sensitive to pair correlations alone.

was thus 6.4 Å at 100 kV and 8.7 Å at 200 kV. Gatan Digital Micrograph v2.0 software was used to collect and process the data. High-band-pass Fourier filtering was used to reduce shot noise, reducing the actual spatial resolution to 25.6 Å for the 100 kV data and 17.4 Å for the 200 kV data. Additional low-band-pass Fourier filtering removed background variations and long-wavelength structure, so that only those wavelengths up to twice the pixel 'fundamental' were present in the filtered images from which S was measured. This CCD system has the attraction of linear response but has a finite point-spread function that can be readily measured and removed (de Ruijter & Weiss, 1992). The expected contribution to the image standard deviation from shot noise was subtracted from the image statistics but attempts were made to keep the average number of counts per CCD pixel constant (typically 1000) in a given series, to minimize variations due to shot
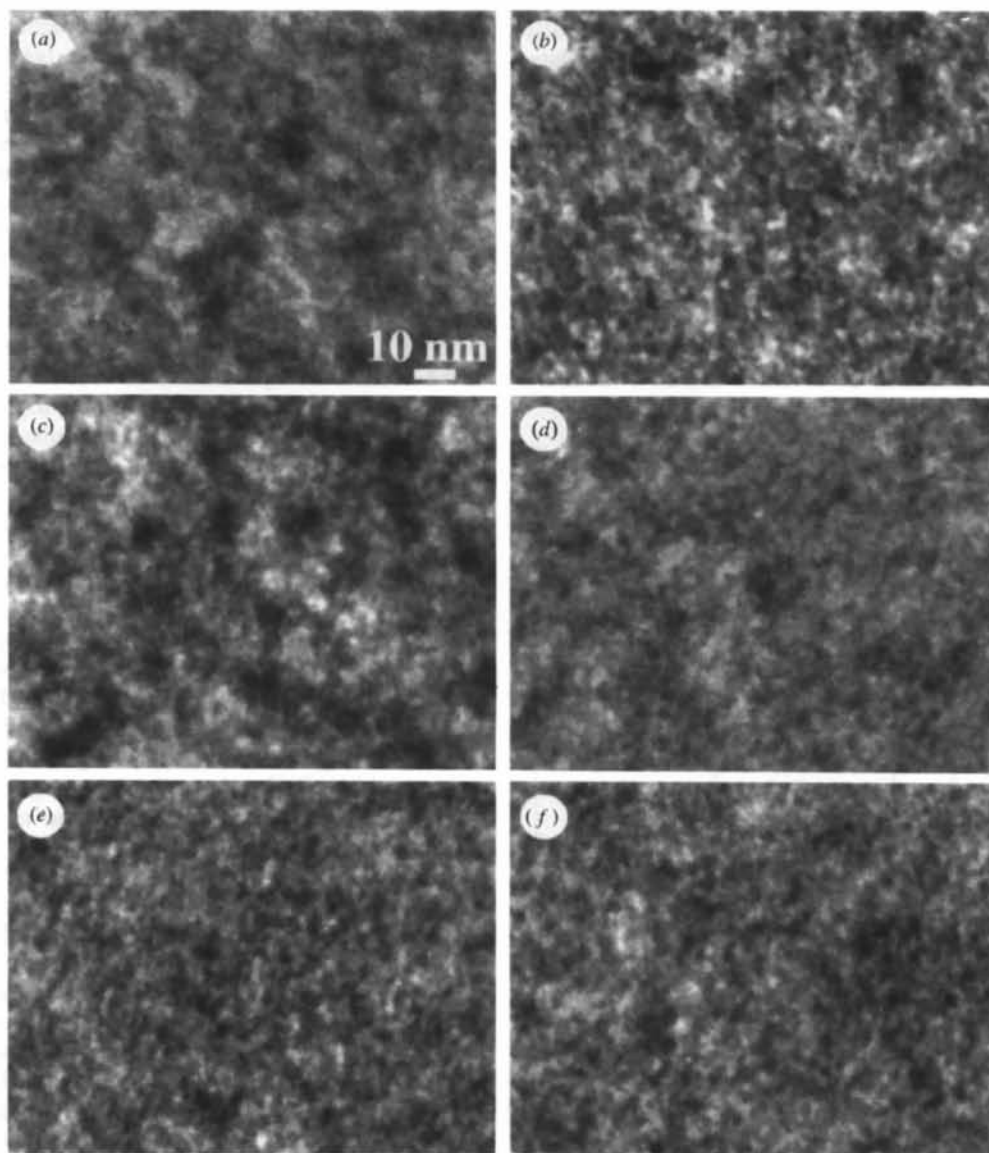

Fig. 2. A series of experimental hollow-cone dark-field images from a 144 Å thick amorphous Ge film for different values of the coherence parameter set by the angle of the hollow-cone illumination (expressed as a reciprocal-lattice vector). The appropriate values are (a) 0.21 Å^{-1}, (b) 0.24 Å^{-1}, (c) 0.30 Å^{-1}, (d) 0.36 Å^{-1}, (e) 0.41 Å^{-1} and (f) 0.43 Å^{-1}. The images were taken at 100 kV using a condenser aperture of semi-angle 5.5 mrad (0.15 Å^{-1}) and an objective aperture of semi-angle 2.2 mrad (0.06 Å^{-1}). The variations in speckle contrast can be seen visually, for example, a peak occurs near $k = 0.25$ Å^{-1} but are best depicted quantitatively (such as in Fig. 4, which describes similar conditions for a thicker Ge film). Note – these images were not taken from the same sample region.

noise. Experiments were not performed at the maximum accelerating voltage of the Hitachi H9000 NAR, 300 kV, because of excessive noise on the CCD camera caused by energetic stray X-rays striking the scintillator. Image noise from X-rays is negligible at 200 kV and below for the typical exposure times ($\leq$ 10 s) used in this study.

4. Results and discussion

Fig. 2 shows a subset of images from a typical series at 100 kV revealing the speckle and how it depends on the hollow-cone tilt vector k. The images are displayed with the same mean intensity and absolute contrast. Even visually, one can see that the speckle variance changes between images. For example, there is maximum speckle in Fig. 2(b). The speckle in images is quantified by the simple measure of the normalized speckle standard deviation S (defined above). This parameter is the focus of this paper, although one could imagine measuring more complex features such as higher-order moments or correlation functions etc. S (in %) is measured as a function of the average semi-angle α of the hollow-cone illumination. For our purposes, it is most useful to use the reciprocal-lattice-vector component $k = \sin(\alpha)/\lambda \simeq \alpha/\lambda$ as the abscissa in our graphs.

Fig. 3 shows the variation in S from a 230 Å thick annealed amorphous Ge film for both 100 and 200 kV. The objective-aperture sizes correspond to image resolutions of 3.1 Å (100 kV) and 4.1 Å (200 kV) using the Rayleigh criterion and ignoring microscope aberrations. The effective pixel size used in the measurements, after band-pass filtering, was 17.4 Å at 200 kV and 25.6 Å at 100 kV. Approximately 120 images were analyzed for each plot and the error bars represent the dispersion of the data and not the error in the average, which is smaller. During exposure of these images, care was taken to keep beam damage to a minimum by not dwelling for too long on any one specimen area. Beam damage was significant over long beam exposures but was found to lead primarily to changes only in the low-frequency structure of the images. Additional low-frequency information, owing to void networks that can be seen in bright-field images, did not contribute to the filtered speckle data. Fig. 3 reveals clear and unambiguous oscillations in S vs the coherence parameter k. A pronounced dip occurs at $k \simeq 0.8$ Å^{-1} in both the 100 and 200 kV data. Strikingly, the data are very similar at 100 and 200 kV, indicating that S scales with k, rather than with $\lambda k^2/2$, thereby implying that the σ_{jl} pair–pair correlations dominate the speckle. Prior to annealing the Ge film, the results were less reproducible and the dip was less pronounced. Results from films of thickness 144 and 230 Å were almost identical.

Fig. 4 shows another plot of S vs k using smaller objective-aperture sizes ($i.e.$ lower image resolution owing to a larger Airy-disc size). In this case, the effective resolutions are 17.4 Å at 200 kV and 8 Å at 100 kV. For

this case, the curves do not scale with k as for the data in Fig. 3. The curves are also found to be relatively independent of thickness for the 144 and 230 Å samples, at least in the position of the oscillations. The 230 Å sample was later tilted by 15 and 20° to check for anisotropy, but no systematic differences were detected. Fig. 5 shows the experimentally determined average intensity for conditions used in Fig. 3. This is identical to the diffraction pattern averaged over the 0.09 Å^{-1} semi-angle condenser aperture and the 0.07 Å^{-1} objective aperture, and is essentially similar to previously reported diffraction patterns from annealed amorphous Ge (Temkin, Paul & Connell, 1973; Graczyk & Chaudhari, 1978).

We obtained the coordinates of a 4096-atom CRN model for amorphous Ge and Si from Fred Wooten (Wooten, Winer & Weaire, 1985). This model was generated from an initial crystalline lattice by permutation of bonds. It has been shown to fit well with the experimental radial distribution function. Spherical models were cut from the CRN for the purpose of our calculations. The radius used in Figs. 6 and 7 was 16 Å, containing 753 atoms. Figs. 6 and 7 show calculations made with the CRN model for the same experimental conditions used in obtaining the data in Figs. 3 and 4, respectively. In comparing these simulations with data, we should first note that the absolute values of
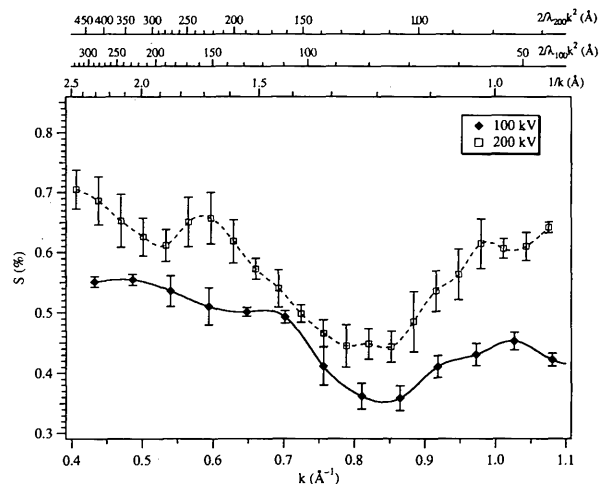

Fig. 3. Experimental data for the normalized speckle standard deviation, S (in %), $versus$ the hollow-cone average effective reciprocal-lattice vector $\mathbf{k}$ (in Å^{-1}) for two values of the accelerating voltage. The sample was a 230 Å thick amorphous Ge film. The condenser apertures, which define the angular spread in the hollow-cone illumination, were 2.25 mrad ($k = 0.09$ Å^{-1}) at 200 kV and 2.2 mrad ($k = 0.06$ Å^{-1}) at 100 kV. The objective-aperture sizes were 5.2 mrad semi-angle (0.21 Å^{-1}) at 200 kV and 5.5 mrad (0.15 Å^{-1}) at 100 kV. The upper three axes indicate the characteristic length scales of the coherence volume as a function of k for the two voltages. As explained in the text, the characteristic lateral periodicity is given by $1/k$, and the characteristic periodicity along z is $2/(\lambda k^2)$.

S should be reduced between the simulations and the experiment by the square root of the number of clusters in an 'imaging column'. This column has a volume given by the product of the area of the image pixel and the thickness of the sample. For the 16 Å radius clusters in this calculation under the imaging conditions used at 200 kV, there would be approximately 13 clusters so that the speckle standard deviation would be reduced by a factor of about 3.6. This puts the 200 kV data in Fig. 6 in quite reasonable agreement with experiment, as far

as approximate magnitude is concerned. For 100 kV, the correction factor is about 2.6.

Apart from the absolute magnitude, there is other notable agreement between experiment and theory. First, both show oscillations. Second, for the 'high-resolution' data (Figs. 3 and 6), both experiment and theory scale

Fig. 6. Theoretical simulation for the normalized speckle standard deviation using a CRN model for amorphous Ge due to Wooten, Winer & Weaire (1985). The conditions in the simulation are exactly as for Fig. 3. The simulation assumes that the sample is composed of randomly oriented but otherwise identical spherical clusters (of radius 16 Å in this case). The simulation uses the column approximation and the kinematical theory and the resulting S must be multiplied by the approximate number of clusters in a column of the sample defined by the effective image pixel size and specimen thickness.
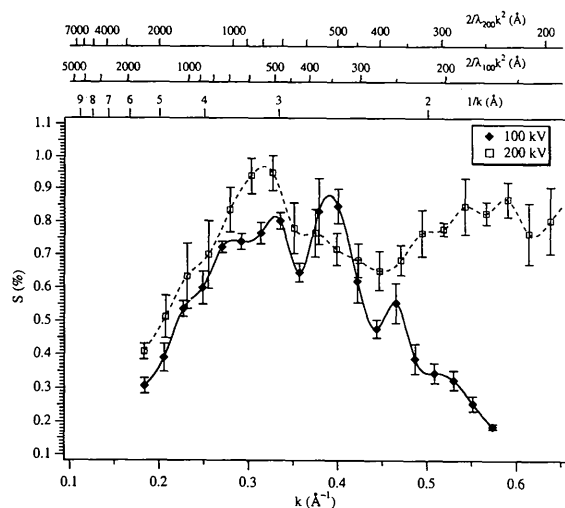

Fig. 4. Experimental data for the normalized speckle standard deviation, S (in %), versus the hollow-cone average effective reciprocal-lattice vector $\mathbf{k}$ (in Å^{-1}) for two values of the accelerating voltage. The sample was a 230 Å thick amorphous Ge film. The condenser apertures, which define the angular spread in the hollow-cone illumination, were 2.25 mrad ($k = 0.09$ Å^{-1}) at 200 kV and 2.2 mrad ($k = 0.06$ Å^{-1}) at 100 kV. The objective-aperture sizes were 1.75 mrad semi-angle (0.07 Å^{-1}) at 200 kV and 1.9 mrad (0.05 Å^{-1}) at 100 kV.
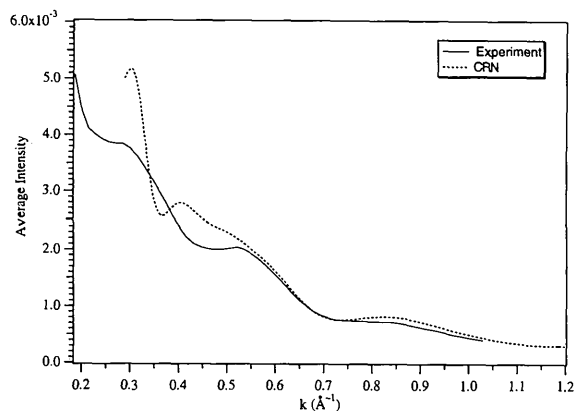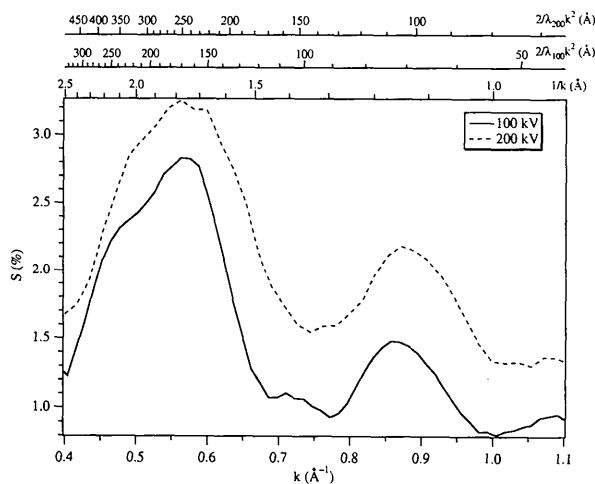

Fig. 5. The experimental average image (average diffracted) intensity using the conditions of Fig. 4 at 200 kV compared to the theoretical prediction of the CRN model of Wooten, Winer & Weaire (1985) under the same conditions.
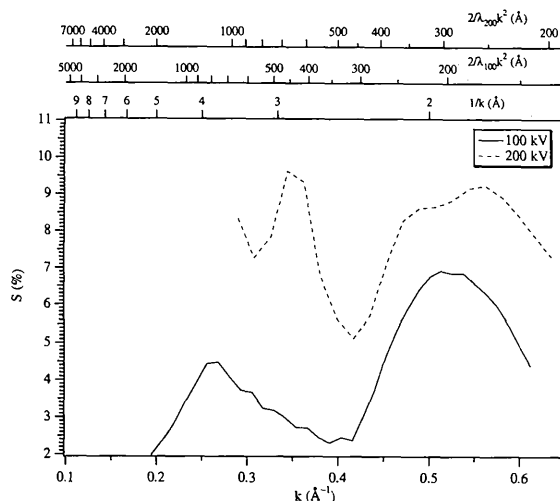

Fig. 7. Theoretical simulations of the normalized speckle standard deviation from a CRN model as for Fig. 6, but calculated under conditions appropriate for Fig. 4, involving smaller objective apertures.

with k for different voltages. In contrast, neither experiment nor theory show k scaling (or λk^2 scaling) in the low-k regime ($k \leq 0.3\,\text{Å}^{-1}$) for the 'lower-resolution' case (Figs. 4 and 7). The detailed peak positions do not, however, agree well with theory.

There is a clear dip present in the data at $0.83\,\text{Å}^{-1}$ (Fig. 3), whereas a similar dip is seen in the model simulations at a lower frequency of $0.74\,\text{Å}^{-1}$ (Fig. 6). We have carefully checked the k calibrations for the experiments and are certain that these are accurate to about $\pm 3\%$, significantly less than the discrepancy. The average image intensity shown in Fig. 5 reveals that the model and experiment agree well in this region, although less well at lower k (the model has more pronounced oscillations). The average image intensity (Fig. 5) shows a dip near $0.74\,\text{Å}^{-1}$, in good agreement with the dip in S seen in simulations. In other words, whereas theory predicts that $\langle I^2 \rangle$ and $\langle I \rangle^2$ track each other in this k regime, as might be expected for truly random fluctuations, experiment does not support this. Perhaps this warrants further theoretical investigation.

From our theoretical discussion, we know that the k scaling observed in Figs. 4 (experiment) and 7 (theory) reveal that σ_{jl} correlations are dominant in this regime. This can be rationalized because in a randomly oriented sample there are many more ways statistically for pairs to line up in a plane when compared to the line direction normal to the plane. This fact more than compensates for the relatively rapid decay of the $F(\sigma_{jl})$ term, a fact that was not noticed in earlier work (Gibson & Howie, 1978). Only when a sample contains significant anisotropy could the z_{jl} correlations dominate and we have no strong evidence for that in this angular regime.

At low k, we observe both experimentally (Fig. 4) and theoretically (Fig. 7) no k scaling with voltage. The theoretical explanation of this is straightforward. At these k values, the Airy amplitudes A_j, centered at each scatterer, are comparable in dimension along σ_j with the width of the coherence strength F_j and it is the 'beating' of these two that gives Bessel-function-like oscillations with k. However, this occurs only if there is structure in the sample at this length scale, i.e. there must be significant fluctuations in the structure on the length scale of the Airy-disc width (the instrument resolution). We confirmed this fact from simulations of truly random structures. The peak at low k in Fig. 7 comes from the $16\,\text{Å}$ radius spherical clusters used in the simulations. The Airy-disc width is $17\,\text{Å}$ in this case, and a pronounced peak shows up. In Fig. 4, we see similar structure at $200\,\text{kV}$ with a quasi-period of $\sim 0.14\,\text{Å}^{-1}$, for an objective-aperture full width of $0.14\,\text{Å}^{-1}$. This implies the existence of significant fluctuations in structure (clustering) on the $17\,\text{Å}$ length scale, beyond those in the CRN model. In an earlier TEM study using phase-randomization techniques, Krivanek, Gaskell & Howie (1976) found no clear evidence for medium-range ordering in their Ge samples, although they did

report ordering on the $\sim 15\,\text{Å}$ scale in amorphous carbon. However, previous small-angle X-ray scattering (Cargill, 1972) has revealed anisotropic medium-range structure in similar films to those studied here. The speckle method should theoretically be much more sensitive than small-angle X-ray scattering and the speckle is not due to simple density fluctuations or voids, which show the same S independent of k.

5. Conclusions

We have shown that variable coherence microscopy is potentially a rich technique for probing correlations in partially disordered materials. This approach provides a quantitative method for studying TEM images, albeit computationally intensive. Naturally, the technique reveals fluctuations, in contrast with diffraction which detects the average structure.

We used variable coherence microscopy to study annealed evaporated amorphous germanium films. While the continuous random network (CRN) model predicts the fluctuations seen in short-range order reasonably well, there is evidence for medium-range correlations in our samples, of length scales $10\text{–}20\,\text{Å}$, which are not present in the CRN.

Finally, we suggest three directions for further research. (a) Better models must be developed for disordered systems. (b) More extensive experiments are needed on other amorphous samples, including Ge. (c) More efficient experimental methods need to be developed to extract microstructural parameters, such as pair–pair correlation functions, directly from the data, particularly when specimens are electron-beam sensitive.

References

Bell, R. J. & Dean, P. (1972). *Philos. Mag.* **25**, 1381–1398.
Cargill, G. S. (1972). *Phys. Rev. Lett.* **28**, 1372–1375.
Chaudhari, P. & Graczyk, J. F. (1973). *Proc. 5th International Conference on Amorphous and Liquid Semiconductors*, Vol. 1, p. 59. London: Taylor and Francis.
Elliott, S. R. (1992). *J. Phys. Condens. Matter*, **4**, 7661–7678.
Fan, G. Y. & Cowley, J. M. (1985). *Ultramicroscopy*, **17**, 345–356.
Fan, G. Y. & Cowley, J. M. (1988). *Ultramicroscopy*, **24**, 49–60.
Gibson, J. M. (1994). *Ultramicroscopy*, **56**, 26–31.
Gibson, J. M. & Howie, A. (1978). *Chem. Scr.* **14**, 109–116.
Gladden, L. F. (1990). *J. Non-Cryst. Solids*, **119**, 318–330.
Graczyk, J. F. & Chaudhari, P. (1978). *Appl. Phys. Lett.* **32**, 466–468.

Jesson, D. E. & Pennycook, S. J. (1993). *Proc. R. Soc. London Ser. A*, **441**, 261–281.

Krakow, W. & Howland, L. A. (1976). *Ultramicroscopy*, **2**, 53–67.

Krivanek, O. L., Gaskell, P. H. & Howie, A. (1976). *Nature (London)*, **262**, 454–457.

Polk, D. E. (1971). *J. Non-Cryst. Solids*, **5**, 365–376.

Polk, D. E. & Boudreaux, D. S. (1973). *Phys. Rev. Lett.* **31**, 92–95.

Ruijter, W. J. de & Weiss, J. K. (1992). *Rev. Sci. Instrum.* **63**, 4314–4321.

Temkin, R. J., Paul, W. & Connell, G. A. N. (1973). *Adv. Phys.* **22**, 581–641.

Treacy, M. M. J. & Gibson, J. M. (1993). *Ultramicroscopy*, **52**, 31–53.

Treacy, M. M. J. & Gibson, J. M. (1995). *J. Microsc.* **180**, 2–11.

Warren, B. E. (1959). *X-ray Diffraction*. Reading, MA: Addison–Wesley.

Wooten, F., Winer, K. & Weaire, D. (1985). *Phys. Rev. Lett.* **54**, 1392–1395.

Zachariasen, W. H. (1932). *J. Am. Chem. Soc.* **54**, 3841–3851.